13th International Symposium on Turbulence and Shear Flow Phenomena (TSFP13)
Montreal, Canada, June 25–28, 2024

TURBULENT TWO-PHASE FLOWS IN A TRANSCRITICAL CO_2 RANQUE-HILSCH VORTEX TUBE

Raphaël Oberti, Antoine Metsue, Yu Fang, Sébastien Poncet*
Mechanical Engineering Department, Université de Sherbrooke
Sherbrooke (QC), J1K 2R1, Canada
*Sebastien.Poncet@USherbrooke.ca

ABSTRACT

The Ranque-Hilsch vortex tube (RHVT) is a topic of a renewed interest as a robust expansion device able to produce also thermal energy separation. With the phase-out of usual refrigerants, carbon dioxide gets more attractive as an environmentally friendly refrigerant. 3D numerical simulations are here performed to better understand the physical mechanisms responsible for the RHVT intriguing behavior. The open-source density-based SU2 solver is coupled to the homogeneous equilibrium (HEM) model and two turbulence closures. The CO_2 properties are evaluated using a fast tabulated real gas approach based on the Span-Wagner equation of state. The solver is first validated against experimental data in transcritical CO_2 de Laval nozzles. Then, an in-depth analysis of the mean and turbulent flow fields in a transcritical CO_2 RHVT is performed before investigating the energy separation.

INTRODUCTION

Transcritical carbon dioxide (CO_2) heat pump cycle is a promising candidate as a sustainable heating and cooling alternative for the decarbonation and efficient electrification of buildings and industrial processes. CO_2 is one of few natural refrigerants to combine competitive cost, non-flammability, non-toxicity, zero ozone depletion and negligible global warming potential. However, the cycle has to operate under transcritical conditions for ambient temperatures higher than its low critical temperature (31.1°C). It yields significant expansion losses resulting from flow irreversibilities through the throttling valve. Therefore, substitutes are required to reduce these losses and improve the cycle efficiency.

The Ranque-Hilsch vortex tube (RHVT) is a mechanical device, which produces energy separation after the tangential injection of a pressurized fluid, generally a gas, into a cylindrical tube. Though this mechanism remains unclear, the vortex tube has found a multitude of applications (Zhang & Guo, 2018) due to its numerous advantages: no moving wall, low-cost ... Recently, using a real gas CO_2 thermodynamic model, Mansour *et al.* (2023) demonstrated the benefit of integrating a RHVT in a transcritical CO_2 heat pump. They obtained an overall heating coefficient of performance up to 43.7% higher by rising the vortex tube hot outlet total pressure and concluded that, despite some limitations, the vortex tube is definitely capable of improving the CO_2 heat pump performance.

The literature on numerical simulations of CO_2 RHVT is scarce due to the complex nature of the flow and energy fields and the inability of commercial solvers to deal with real gas properties and density-based solver at the same time. Baghdad *et al.* (2012) and Aghagoli & Sorin (2019) used high-Reynolds number turbulence closure available in ANSYS Fluent coupled to a pressure-based solver though the Mach number far exceeded the incompressibility limit. In a former paper, Oberti *et al.* (2023) benchmarked the performance of the perfect gas, the Peng-Robinson and the Span and Wagner equations of state under subcritical conditions, on the outlet total pressure and temperature metrics, using the $k-\omega$ SST turbulence closure at multiple cold mass fractions (μ_c). However no attempt has been done so far for CO_2 RHVT under transcritical conditions. This paper provides the first 3D CFD investigation of compressible two-phase transcritical CO_2 flows inside a RHVT.

NUMERICAL METHOD

The 3D governing equations for the conservation of mass, momentum and energy for a compressible turbulent flow, i.e. the Favre-averaged Navier-Stokes equations, are solved using the open-source unstructured code SU2 7.5.0 (Economon *et al.*, 2016). Based on the finite volume method, it includes a density-based solver, with a non-ideal gas formulation and a fully implicit Euler time integration. The spatial discretization is based on the dual-grid vertex-based method. The approximate Riemann solver of Roe in its real gas formulation is selected for the convective fluxes (Vitale *et al.*, 2015) and the weighted least-squares method is employed to evaluate the gradients for the viscous fluxes. A second-order spatial accuracy is obtained using the monotonic upwind scheme for conservation laws (MUSCL) along with the Venkatakrishnan slope limiter (Venkatakrishnan, 1995). The homogeneous equilibrium model (HEM), which is a compressible two-phase model assuming mechanical and thermodynamic equilibria, is selected. With this model, liquid-vapor phase change and consequently equilibrium is assumed to be instantaneous. Two two-equation turbulence closures, namely the $k-\omega$ SST and Std (standard) $k-\varepsilon$, are compared.

A look-up table method based on the Span and Wagner equation of state (EOS) is used to compute the CO_2 properties from the triple point temperature, 216.59 K, up to 500 K with pressures up to 50 MPa (Fang *et al.*, 2018). The maximum relative errors between the original Span and Wagner EOS and the tabulated values are: 0.23 % on pressure, 0.06 K on temperature and 1.2 % on sound speed. The tabulated method was found to be up to 66 faster than the original EOS. The interested reader is referred to Fang *et al.* (2018) for further details about the tabulated CO_2 EOS.

RESULTS AND DISCUSSION

Validation with nozzle flows

Due to the absence of reliable experimental data for transcritical CO_2 vortex tubes, the solver validation is performed with nozzle flows considered by Lettieri *et al.* (2018) and Nakagawa *et al.* (2009), who carried out high-pressure CO_2 nozzle experiments for comparable operating conditions. Table 1 summarizes the three selected cases from Lettieri *et al.* (2018) including the inlet stagnation temperature T_{0in} and pressure p_{0in} as well as the outlet static pressure p_{out}. For the nozzle of Nakagawa *et al.* (2009), constant inlet operating conditions of 310.15 K and 9 MPa, with an increasing diffuser angle were selected and named nozzle 1, 2 and 3 respectively. A mesh grid composed of 46 k (resp. 21 k) structured hexahedral cells is used in the simulations leading to $y^+ < 1$ (resp. $y^+ > 30$) for the $k-\omega$ SST (resp. Std $k-\varepsilon$) model.

Table 1. Operating points and boundary conditions for the nozzle of Lettieri *et al.* (2018).

Case	p_{0in} (MPa)	T_{0in} (K)	p_{out} (MPa)
3	7.3	310	2.43
4	8	311	2.67
5	8.4	312	2.88

Figure 1 reports the pressure distributions along the normalized nozzle axis, whose origin is at the throat, for Lettieri *et al.* (2018) (Fig. 1a) and Nakagawa *et al.* (2009) (Fig. 1b) experiments. On Fig. 1a, for both near-wall treatments, the pressure profile matches very well before condensation onset, with less than 1.7% mean relative error. Then, both closures under-predict the pressure post-condensation onset, with 11.4% and 8.2 % errors for the $k-\omega$ SST and the Std $k-\varepsilon$ models, respectively. As the present inlet conditions depart from the critical point, non-equilibrium phase change involving metastable CO_2 vapor could be produced, as mentioned by the authors of the experiments (Lettieri *et al.*, 2018), which is not accounted for with the HEM, by definition. Nevertheless, the present results improve the two-fluid CFD model of Sahu *et al.* (2022), who reached 18.4% mean relative error post-condensation onset on case 3. The results further indicate that the Std $k-\varepsilon$ model matches better the experimental pressure profile than the $k-\omega$ SST in the first half of the diffuser for all cases, after which pressure oscillations appear. The higher post-condensation onset pressure of the first compared to the second model can be explained by the higher numerical diffusion yielding thicker boundary layers which, by conservation of mass, leads to a lower stream-wise velocity in supersonic regime. Similar relative errors are obtained with Nakagawa *et al.* (2009) nozzles. In this case, the pressure trends are fairly accurate with the experimental saturation pressures and less accurate with regard to the experimental wall pressures with the 3 diffuser geometries. This can be due to the HEM equilibrium assumption where the two-phase pressure field is equal to the saturation pressure computed from the temperature field.

Ranque-Hilsch vortex tube

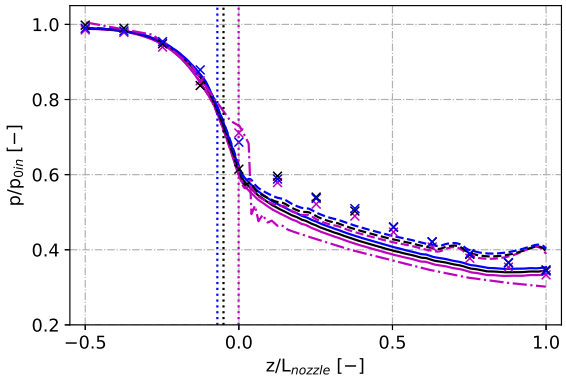

(a)

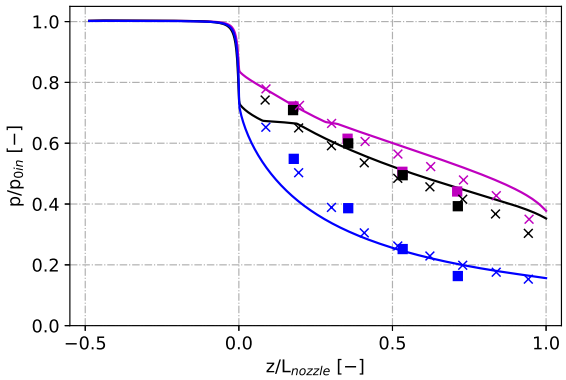

(b)

Figure 1. Normalized pressure profiles in the nozzles of (a) Lettieri *et al.* (2018) and (b) Nakagawa *et al.* (2009). Experimental pressure at the wall (×) and $P_{sat}(T_{wall})$ (□), $k-\omega$ (solid lines), Std $k-\varepsilon$ (dashed lines), predictions of Sahu *et al.* (2022) (dash dotted line) and condensation onset location (dotted lines). Results for case 3 and nozzle 1 (magenta), case 4 and nozzle 2 (black) and case 5 and nozzle 3 (blue).

.

Figure 2 displays the vortex tube geometry, the boundary conditions and the wall-resolved mesh grid, including 50 million unstructured tetrahedral cells, leading to $y^+ < 1$ for all cases modeled in the following using the $k-\omega$ SST closure. The geometry corresponds to the experimental testbench of Zhu (2015). Table 2 provides the supercritical CO_2 inlet operating conditions simulated here.

OP	p_{0in} (MPa)	T_{0in} (K)	μ_c (-)	$p_{c,out}$ (MPa)	$p_{h,out}$ (MPa)
1	9	315	0.24-0.89	4.27-4.95	5.4
2	9	313	0.24-0.88	4.27-4.95	5.4
3	8.5	313	0.25-0.91	4.04-4.46	5.1
4	8.3	310	0.66	4	4.8

Table 2. Vortex tube operating points (OP): inlet ($0in$) and outlet conditions (cold c,out and hot h,out) and cold mass fractions (μ_c: ratio between the cold and inlet mass flowrates).

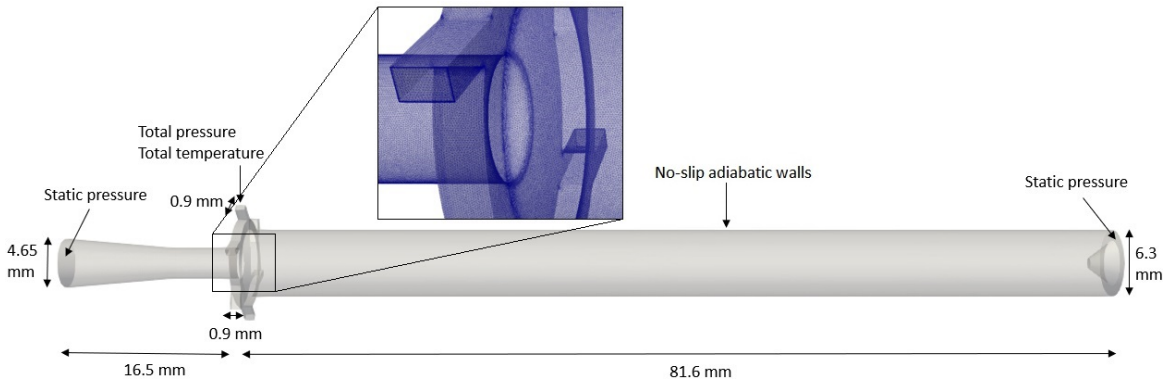

Figure 2. Vortex tube geometry, boundary conditions and wall-resolved mesh grid.

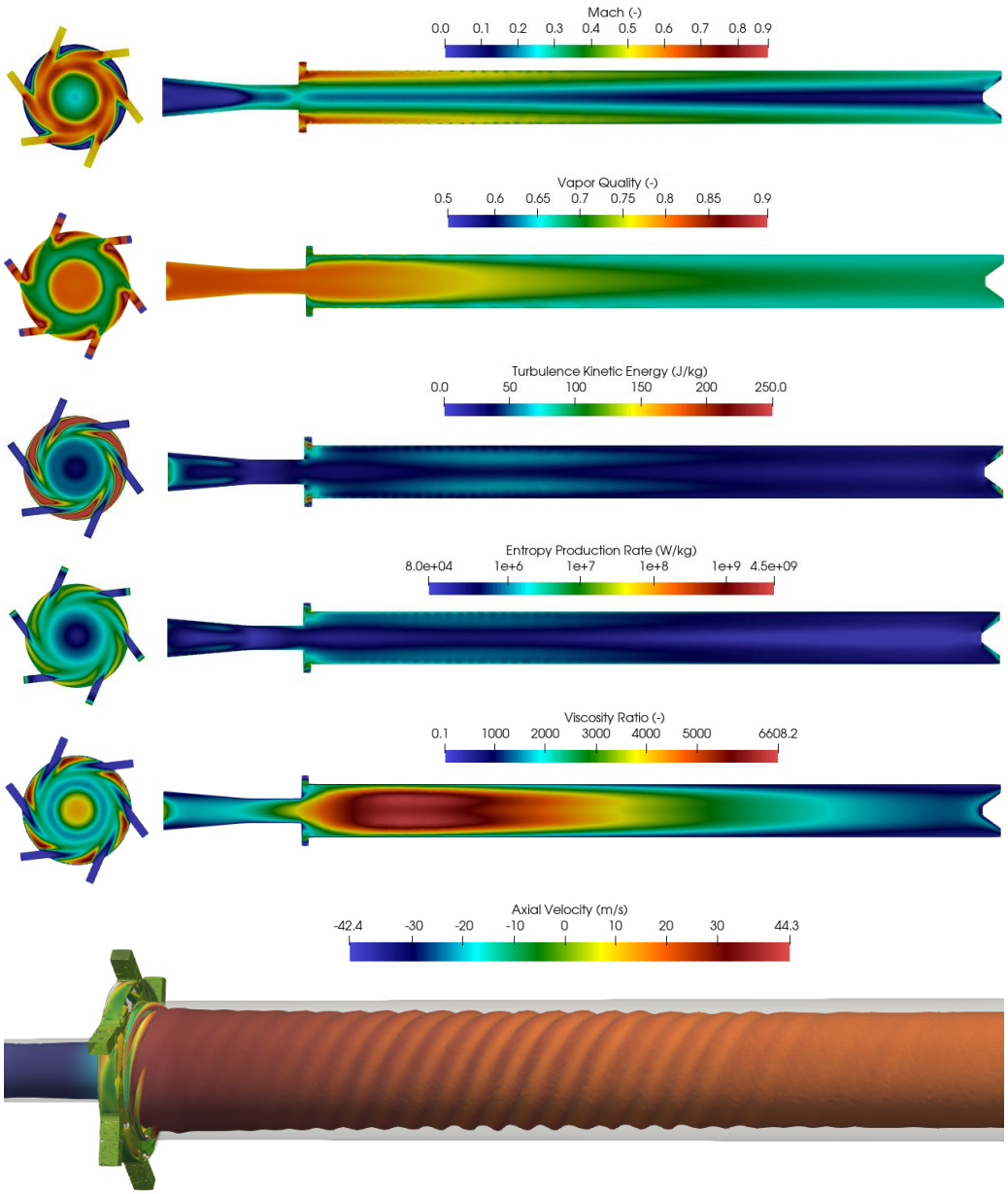

Figure 3. Contours of the Mach number, vapor quality, turbulence kinetic energy, entropy production rate and viscosity ratio in the inlet plane (left) and median plane (right) and iso-surface 10^6 of the Q-criterion colored by the mean axial velocity at OP1.

Figure 3 displays 2D contours of the Mach number, vapor quality, turbulence kinetic energy (TKE), entropy production rate (EPR) and turbulence to molecular viscosity ratio in the inlet plane and along the median plane of the RHVT for OP1. The results show first the compressibility effects, which are more important close to the inlets, as the Mach number may reach 0.9. It confirms the absolute need for a density-based solver. The high-speed tangential flows at the 6 inlets convert in an axial flow confined along the RHVT external wall. The spindle at the hot exit (on the right), which enables to control the μ_c value, creates a back flow coming back to the cold exit (on the left) along the RHVT axis. The vapor quality remains within the $[0.5-0.9]$ range, showing the two-phase nature of the flow. It reaches a maximum at the cold outlet (left) where the temperature drops to 284.5 K. It is noteworthy that even the hot outlet is colder (292.2 K) than the inlet under transcritical conditions. TKE is maximum between 2 successive inlet pipes and remains relatively low in most of the RHVT. A region of higher TKE values is also obtained along the reverse flow boundary, where the EPR is maximum. It is further observed that the turbulence viscosity overcomes the molecular viscosity by a factor 6.6×10^3. This suggests that the flow energy is dissipated by turbulence rather than the fluid itself. The maximum values are reached between 2 successive inlet pipes as well as in the main tube on both sides of the central axis, where most of the RHVT energy separation usually takes place. This gives an insight on the possible link between energy separation and turbulent viscous dissipation which will be discussed in the following. Figure 3 presents also an isosurface of the Q-criterion colored by the mean axial velocity. Apart from spiral patterns at the outlets of the inlet nozzles, it reveals some helicoidal structures in the hot flow going to the right of the vortex tube, which weaken towards the hot outlet. These structures are responsible for the oscillations observed on the Mach number contours along the external wall.

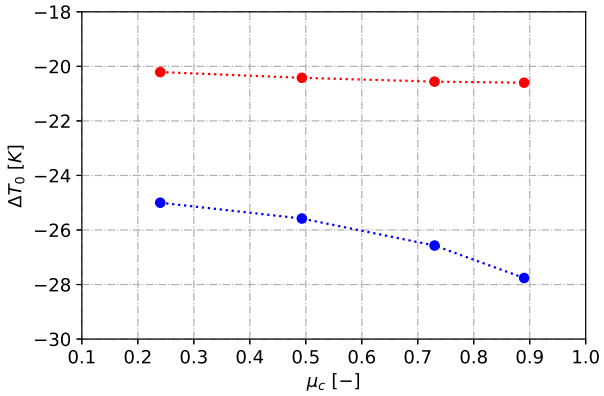

Figure 4. Total temperature separations on the cold (blue) and hot (red) outlets at OP1.

Figure 4 displays the total temperature separation $\Delta T_0 = T_{out,h} - T_{0in}$ on the hot and $\Delta T_0 = T_{out,c} - T_{0in}$ cold sides as a function of the cold mass fraction μ_c. The negative values confirm what has been observed for single-phase CO_2 vortex tubes (Oberti & Poncet, 2023). The temperature separation occurs below the inlet temperature T_{0in}, which is expected on the cold side. On the hot side, this peculiar behavior is a consequence of the thermodynamic conditions. The isenthalpic expansion near the critical point provokes a decrease of the static temperature due to the nearly horizontal shape of the isotherms in the CO_2 $p-h$ diagram. The hot outlet temperature can not then exceed the inlet temperature due to real gas effects.

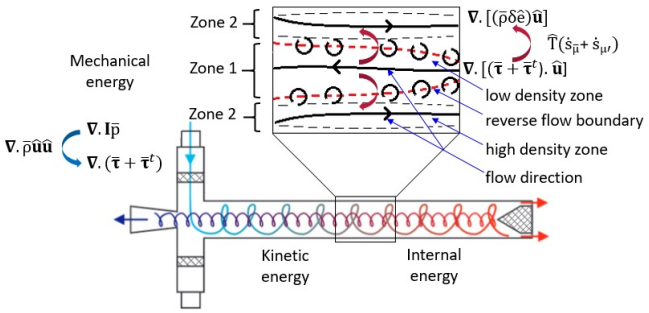

Figure 5. Suggested Ranque-Hilsch vortex tube energy transfer process via entropy production at the reverse flow boundary (zero axial velocity). Lower and higher internal energy density areas correspond to zone 1 (core vortex) and zone 2 (peripheral vortex), respectively.

Figure 5 is a schematic of the suggested energy transfer process within the RHVT. Terms $\dot{s}_{\overline{\mu}}$ and $\dot{s}_{\mu'}$ represent the entropy production rate due to the mean-flow and fluctuating viscous dissipations, respectively. They can be obtained from the entropy transport equation and approximated as:

$$\dot{s}_{\overline{\mu}} = \frac{1}{\hat{T}}\overline{\tau} : (\nabla\hat{u})^T \tag{1}$$

$$\dot{s}_{\mu'} = \frac{\overline{\rho}\varepsilon}{\hat{T}} \tag{2}$$

where the product between the mean-flow viscous stress tensor and strain rate, in Eq. (1), is only a function of the Favre-averaged velocity gradients and the molecular viscosity. The Favre-averaged turbulence dissipation rate $\overline{\rho}\varepsilon$, in Eq. (2), is positive-definite and represents a dissipation of TKE as it appears as a sink term in the Favre-averaged TKE equation (Wilcox, 2006). Then, the integral entropy production due to viscous dissipation can be interpreted as the irreversible work done by the fluid due to the strain rate against the viscous stresses and can be defined as:

$$\dot{S}_{prod} = \int_\Omega \hat{T}(\dot{s}_{\overline{\mu}} + \dot{s}_{\mu'})\, d\Omega \qquad [W] \tag{3}$$

where $d\Omega$ is the control volume.

Figure 6 displays the radial profiles of the local entropy production rates $\dot{s}_{\overline{\mu}}$ and $\dot{s}_{\mu'}$ at OP1 for $\mu_c = 0.24$ and 0.89. The fluctuating contribution overcomes the mean one by orders of magnitude for all operating points and cold mass fractions. Both contributions reach a minimum in the core, along

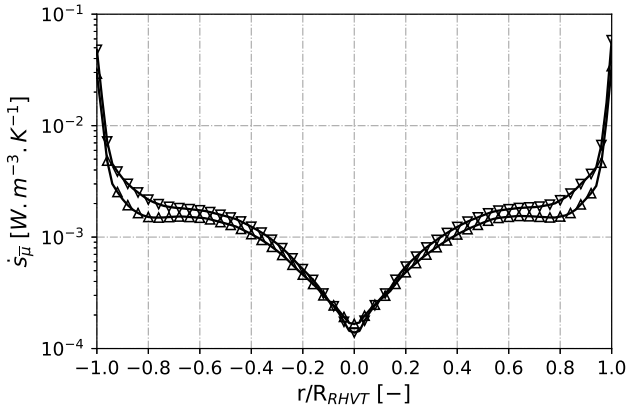

(a)

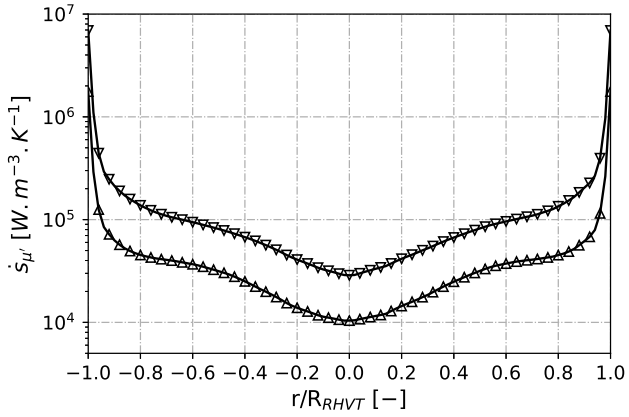

(b)

Figure 6. Radial profiles of the local entropy production rates (a) $\dot{s}_{\overline{\mu}}$ and (b) $\dot{s}_{\mu'}$. Results for OP1 at $z/L_{RHVT} = 0.4$ and two values of the cold mass fraction $\mu_c = 0.24$ ($\bigtriangledown$) and $\mu_c = 0.89$ ($\bigtriangleup$).

the vortex chamber axis ($r/R_{RHVT} = 0$), and get maximum along the walls. For $0.5 \leq r/R_{RHVT} \leq 0.7$, corresponding to the reverse flow boundary, the two terms are almost constant.

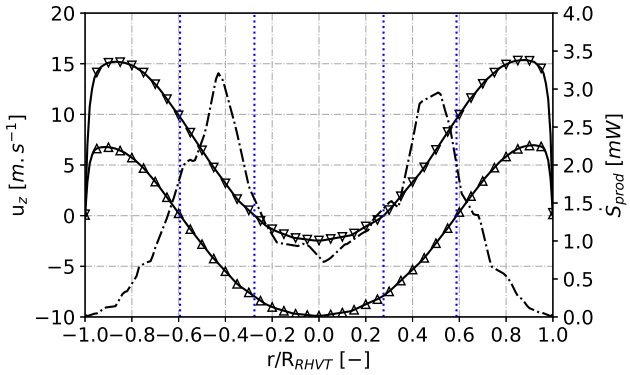

Figure 7. Radial profiles of the mean axial velocity u_z for OP1, $z/L_{RHVT} = 0.4$ at $\mu_c = 0.24$ ($\bigtriangledown$) and $\mu_c = 0.89$ ($\bigtriangleup$) and integral entropy production at the cell level $\dot{S}_{prod}$ at μ_c = 0.49 (dash dotted line). The blue dotted lines stand for the zero axial velocity (reverse flow boundary).

Figure 7 shows the radial profiles of the integral entropy production at the cell level $\dot{S}_{prod}$ at μ_c = 0.49. The peak values fall into the reverse flow boundary region delimited by the vertical blue dotted lines. Also, the smaller the cold mass fraction the weaker the cold backflow towards the left along the axis. The axial velocity gradients in the reverse flow boundary region are more important, which favors turbulent dissipation, rising the integral entropy generation.

Coming back to Figure 5, energy is injected in the vortex tube under the form of mechanical energy (pressure) and converts into kinetic energy contained in the tangential flow (velocity). The flow in the vortex chamber is divided into two regions: (i) zone 1 characterized by low density and low internal energy, (ii) zone 2 characterized by high density and high internal energy. These are separated by the so-called reverse flow boundary. The integral entropy production is maximum along that boundary ($0.5 \leq r/R_{RHVT} \leq 0.7$) and gets larger at larger cold mass fractions. This is accompanied by a larger temperature / energy separation. One possible explanation for the separation phenomenon is therefore the dominating contributions of the turbulent viscous and heat dissipations by smaller eddies.

CONCLUSION

Numerical modelings of a two-phase turbulent flow inside a transcritical CO_2 Ranque-Hilsch vortex tube have been performed using the open-source SU2 FANS solver coupled to a fast tabulated version of the Span and Wagner equation of state, the HEM and two turbulence closures (St $k-\varepsilon$ and $k-\omega$ SST). The model has been first carefully validated against experimental data for transcritical CO_2 nozzle flows. Then 4 operating transcritical conditions (and multiple cold mass fractions for each of them) have been considered for the RHVT of Zhu (2015). The detailed analysis of the fluid flow, heat transfer and entropy production revealed the prime importance of the reverse flow region inside the RHVT formed because of a combination of viscous dissipation at the external walls and adverse pressure gradient produced by the hot end spindle. One explanation for the temperature/energy separation has been provided: turbulent viscous and heat dissipations are maximum along the reverse flow boundary. This separation is enhanced at larger cold mass fractions, as the entropy production rate in that region gets higher.

Future works include large eddy simulations to characterize possible unsteady flow patterns and the vortex breakdown and quantify their influence on the vortex tube energy separation phenomenon. The first experimental campaign on transcritical CO_2 vortex tube flows is currently ongoing and will help further validating the present numerical model.

ACKNOWLEDGEMENTS

The authors acknowledge the support of the NSERC chair on industrial energy efficiency established in 2019 at Université de Sherbrooke funded by Hydro-Québec, Natural Resources Canada and Copeland Canada Inc. Computational resources have been provided by Digital Research Alliance of Canada.

REFERENCES

Aghagoli, A. & Sorin, M. 2019 Thermodynamic performance of a CO_2 vortex tube based on 3D CFD flow analysis. *In-*

ternational Journal of Refrigeration **108**, 124–137.

Baghdad, M., Ouadha, A. & Addad, Y. 2012 CFD modelling and exergy analysis of a vortex tube using CO_2 as the working fluid. In *Proceedings of the 10th IIR-Gustav Lorentzen Conference on Natural Working Fluids (GL2012)*. Delft, the Netherlands.

Economon, T. D., Palacios, S., Copeland, S. R., Lukaczyk, T. W. & Alonso, J. J. 2016 SU2: An open-source suite for multiphysics simulation and design. *AIAA Journal* **54**, 828–846.

Fang, Y., De Lorenzo, M., Lafon, P., Poncet, S. & Bartosiewicz, Y. 2018 An Accurate and Efficient Look-up Table Equation of State for Two-Phase Compressible Flow Simulations of Carbon Dioxide. *Industrial & Engineering Chemistry Research* **57** (22), 7676–7691.

Lettieri, C., Paxson, D., Spakovszky, Z. & Bryanston-Cross, P. 2018 Characterization of Nonequilibrium Condensation of Supercritical Carbon Dioxide in a de Laval Nozzle. *Journal of Engineering for Gas Turbines and Power* **140** (4), 041701.

Mansour, A., Oberti, R., Nesreddine, H. & Poncet, S. 2023 Thermodynamic analysis of a transcritical CO_2 heat pump integrating a vortex tube. *Applied Thermal Engineering* **224**, 120076.

Nakagawa, M., Berana, M.S. & Kishine, A. 2009 Supersonic two-phase flow of CO_2 through converging–diverging nozzles for the ejector refrigeration cycle. *International Journal of Refrigeration* **32** (6), 1195–1202.

Oberti, R., Lagrandeur, J. & Poncet, S. 2023 Numerical benchmark of a Ranque–Hilsch vortex tube working with subcritical carbon dioxide. *Energy* **263, Part C**, 125793.

Oberti, R. & Poncet, S. 2023 Thermodynamic paths along the streamlines of a single-phase transcritical CO_2 vortex tube. In *Proceedings of the CSME / CFDCanada 2023 International Congress*, pp. 1–6. Sherbrooke, Canada.

Sahu, K. D., Yadav, S. S. & Dasgupta, M. S. 2022 CFD Simulation of Supercritical Carbon Dioxide in a Converging-Diverging Nozzle. In *Proceedings of the 15th IIR Gustav Lorentzen conference*. Trondheim, Norway.

Venkatakrishnan, V. 1995 Convergence to Steady State Solutions of the Euler Equations on Unstructured Grids with Limiters. *Journal of Computational Physics* **118** (1), 120–130.

Vitale, S., Gori, G., Pini, M., Guardone, A., Economon, T.D., Palacios, F., Alonso, J.J. & Colonna, P. 2015 Extension of the SU2 open source CFD code to the simulation of turbulent flows of fuids modelled with complex thermophysical laws. In *22nd AIAA Computational Fluid Dynamics Conference*. Dallas, United States.

Wilcox, D.C. 2006 *Turbulence modeling for CFD*, 3rd edn. DCW Industries Incorporated.

Zhang, B. & Guo, X. 2018 Prospective applications of Ranque–Hilsch vortex tubes to sustainable energy utilization and energy efficiency improvement with energy and mass separation. *Renewable and Sustainable Energy Reviews* **89**, 135–150.

Zhu, J. 2015 Experimental investigation of vortex tube and vortex nozzle for applications in air-conditioning, refrigeration, and heat pump systems. Master's thesis, University of Illinois at Urbana-Champaign.